Applied Surface Science 366 (2016) 120–128

Contents lists available at ScienceDirect

Applied Surface Science

journal homepage: www.elsevier.com/locate/apsusc

Surface plasmon resonance enhanced visible-light-driven photocatalytic activity in Cu nanoparticles covered Cu_2O microspheres for degrading organic pollutants

Yahui Cheng[a,*], Yuanjing Lin[a], Jianping Xu[b], Jie He[a], Tianzhao Wang[a], Guojun Yu[a], Dawei Shao[a], Wei-Hua Wang[a], Feng Lu[a], Lan Li[b], Xiwen Du[c], Weichao Wang[a], Hui Liu[a,*], Rongkun Zheng[d]

[a] Department of Electronics and Key Laboratory of Photo-Electronic Thin Film Devices and Technology of Tianjin, Nankai University, Tianjin 300071, China
[b] Institute of Material Physics, Key Laboratory of Display Materials and Photoelectric Devices, Ministry of Education, Tianjin University of Technology, Tianjin 300384, China
[c] School of Material Science and Engineering, Tianjin University, Tianjin 300072, China
[d] School of Physics, The University of Sydney, Sydney, NSW 2006, Australia

ARTICLE INFO

Article history:
Received 22 September 2015
Received in revised form
14 December 2015
Accepted 16 December 2015
Available online 6 January 2016

Keywords:
Photocatalysis
Surface plasmon resonance
Cu_2O
Visible-light-driven

ABSTRACT

Micron-sized Cu_2O with different coverage of Cu nanoparticles (NPs) on the sphere has been synthesized by a redox procedure. The absorption spectra show that Cu NPs induce the surface plasmon resonance (SPR) at the wavelength of ~565 nm. Methylene blue (MB) photodegrading experiments under visible-light display that the Cu_2O–Cu–H_2O_2 system exhibits a superior photocatalytic activity to Cu_2O–H_2O_2 or pure H_2O_2 with an evident dependency on Cu coverage. The maximum photodegradation rate is 88% after visible-light irradiating for 60 min. The role of the Cu NPs is clarified through photodegradation experiments under 420 nm light irradiation, which is different from the SPR wavelength of Cu NPs (~565 nm). By excluding the SPR effect, it proves that Cu SPR plays a key role in the photodegradation. Besides, a dark catalytic activity is observed stemming from the Fenton-like reaction with the aid of H_2O_2. The radical quenching experiments indicate that both $\bullet O_2^-$ and •OH radicals contribute to the photocatalysis, while the dark catalysis is only governed by the •OH radicals, leading to a lower activity comparing with the photocatalysis. Therefore, with introducing Cu NPs and H_2O_2, the Cu_2O-based photocatalytic activity could be significantly improved due to the SPR effect and dark catalysis.

1. Introduction

Since the discovery of water splitting on n-type TiO_2 electrodes [1], semiconductor photocatalysts have been extensively studied. Till now, TiO_2 has been proven to be the most successful semiconductor photocatalyst in the environmental and energy-related fields such as water splitting for hydrogen generation, initiating the chemical reactions and degrading the organic pollutants [2–4]. However, the wide bandgap of 3.2 eV restricts its absorption to UV irradiation, which is only less than 5% of the solar energy. The development of photocatalysts with high activity under visible-light will allow the main part (about 46%) of the solar spectrum to be used [2]. Over recent years, there are two main approaches to exploit the visible-light responsive single-phase photocatalysts [5]. One is to modify the TiO_2 by doping other elements or forming the reduced TiO_x [3,6–8], and the other is to develop new types of semiconductors with narrower bandgap, such as α-Fe_2O_3, CdS, $BiVO_4$, WO_3, Cu_2O, and etc. [9–13].

Among the narrow bandgap semiconductor photocatalysts, the cuprous oxide (Cu_2O) with a direct bandgap of 2.17 eV is very attractive because of its unique properties such as p-type character, comparatively negative conduction band position, low-cost, abundance and non-toxicity. In recent years, there is a growing interest to the synthetic, morphological, and catalytic properties of pristine Cu_2O [13–16]. For example, Ho et al. synthesized submicrometer-sized Cu_2O with morphological evolution from cube to hexapod [13]. Photocatalytic tests exhibited no degradation for the MB. Zhang et al. prepared polyhedral Cu_2O microcrystals [15]. The degradation rate of methyl orange is about 30% after visible-light

* Corresponding authors. Tel.: +86 2223509930.
E-mail addresses: chengyahui@nankai.edu.cn (Y. Cheng), liuhui@nankai.edu.cn (H. Liu).

http://dx.doi.org/10.1016/j.apsusc.2015.12.238
0169-4332/

irradiating for 3 h. Kuo et al. fabricated monodispersed Cu_2O truncated nanocubes and octahedra with controllable sizes [16]. The degradation rate of the rhodamine B is only about 30% after 6 h of irradiation. All these results demonstrate that the bare Cu_2O photocatalysts have a limited photocatalytic activity.

In order to improve the photocatalytic activity of Cu_2O, three basic requirements should be further optimized including carriers' excitation, separation, and transportation. Therefore, it is essential to create a composite structure, either the p–n junction (e.g., Cu_2O/TiO_2 [17], Cu_2O/ZnO [18], and Cu_2O/TaON [19]) or the Cu_2O/metal contact [20–24], which have been demonstrated to be potentially effective photocatalysts. Among the composite structure strategies, the Cu_2O/noble metal structure is one of the promising candidates. Taking advantage of the noble metal, the photocatalytic efficiency can be improved greatly by suppressing the charge recombination [25]. Moreover, it has been proved recently that the efficiency can be further enhanced by utilizing the synergistic effect of the surface plasmon resonance (SPR) [20,26–29].

SPR can be characterized as the resonant photo-induced collective oscillation of valence electrons, established when the frequency of surface electrons oscillating against the restoring force of positive nuclei [30]. Incorporating plasmon metal (e.g., Au, Ag, Cu and etc.) into semiconductors will enhance the photocatalytic activity by concentrating electromagnetic fields, scattering the electromagnetic radiation, transferring the plasmonic energy to excite the electron–hole pairs, or directly generating the hot electrons [30–37]. So far, the influence of the Ag and Au induced SPR on the photocatalysis are of particular interest [21,38,39]. However, the noble metal is significantly costly and the reserves are very limited. Therefore, the development of an inexpensive plasmon-metal-based photocatalyst, such as Cu-based photocatalyst, is urgent.

In this work, a composite of Cu_2O microsphere caped with nano-sized Cu particles was proposed. In addition to the charge separation and the SPR effect, this specific Cu_2O–Cu composite presents more advantages. First, compared with the existing metal@Cu_2O and Cu_2O@metal core–shell structure [21,23,24], both Cu_2O and Cu could be irradiated, and the excited carries prefer to stay on the external surfaces. Second, stemming from the smaller work function of Cu than Au, the excited electrons (or holes) are readily moved to Cu (or Cu_2O) surface without resistance from the Schottky barrier, resulting in the improvement of the carrier separation. Third, compared with the SPR in the core–shell structure, isolated nano-sized Cu particles cause the localized surface plasmon resonance (LSPR), and thus lead to several orders of magnitude enhancement of the surface local field when two Cu particles separated by ~1 nm [30]. In the following parts, MB degradation experiments will be carried out to examine the superior catalytic performance. The reaction mechanism is investigated through the radical quenching experiments. These results may be helpful to develop new types of high efficiency photocatalysts for the applications of cleaning the organic pollutants.

2. Experimental

2.1. Materials

Cupric sulfate ($CuSO_4{\cdot}5H_2O$), sodium hydroxide (NaOH), ethylene glycol, H_2O_2 and isopropyl alcohol (IPA) were obtained from Tianjin Jiangtian Chemical Technology Co., Ltd., China. D-Glucose was provided by Tianjin Guangfu Technology Development Co., Ltd., China. Nitroblue tetrazolium (NBT) was purchased from Aladdin Industrial Co., China. Degussa P25 TiO_2 was purchased from Hualisen Trading Co., Ltd., China. All chemicals were of analytical grade and were used as received without further purification. Aqueous solutions were prepared using deionized water.

2.2. Synthesis of Cu_2O–Cu composites

The Cu_2O–Cu composites with different coverage of Cu NPs were synthesized following a facile redox procedure [40]. Details of the synthetic procedures were described as follows: 2 mmol $CuSO_4{\cdot}5H_2O$, 20 ml ethylene glycol, and 10 ml deionized water were added into a conical flask, which was immersed in water bath at 60 °C. The mixture was stirred with a magnetic stirrer for 10 min in order to ensure the ethylene and $CuSO_4$ dissolved completely. Then, 10 ml 5 M of NaOH solution was added in a dropwise manner. After 5 min, 10 ml 1.1 M of D-glucose solution was added into the blue suspension within 30 s. The mixed solution soon turned yellow. The entire reaction was kept at 60 °C for varied periods of reaction (10, 20, 30, 40, 50, 60, and 150 min) under magnetic stirring. A brick-red color appeared gradually. When the reaction finished, the precipitate was separated from the solution by centrifugation at 4000 rpm for 5 min, washed with alcohol and deionized water several times, and dried at 60 °C for 60 min in a vacuum oven. According to the reaction time, the samples were labeled as S10, S20, S30, S40, S50, S60, and S150, respectively.

The contents of metallic Cu in the Cu_2O–Cu composites are determined by titrimetric methods. The specific mass percentage of Cu is ca. 0.5%, 1.2%, 7.5%, 10.2%, 31.7%, 38.4%, and 98.5% for S10, S20, S30, S40, S50, S60, and S150, respectively. The details of the titrimetric methods are shown in the Supplementary data.

2.3. Characterization methods

The phase structures were investigated using X-ray diffraction (XRD, D/max-2500) with Cu $K\alpha$ radiation (λ = 0.15406 nm, 40 kV, 100 mA). The valence states were analyzed by X-ray photoelectron spectroscopy (XPS, Thermo Escalab 250Xi) with Al K_α X-ray source. The morphologies and microstructures of the Cu_2O–Cu composites were characterized by scanning electron microscopy (SEM, S-3500N) and transmission electron microscopy (TEM, JEOL 2200F, Akishima-shi, Japan) operating at 200 kV. UV–vis absorption spectra were acquired with UV–vis spectrophotometer (HITACHI UV-4100).

2.4. Photocatalytic activity tests and electrochemical measurement

The photocatalytic activity was evaluated by the degradation of azo dye MB at a concentration of 10 mg/l under the visible-light. A typical degradation process is as below. 9 mg of Cu_2O–Cu powder were dispersed in 30 ml of dye solution. The suspension was stirred in the dark for 60 min before illumination to achieve an adsorption/desorption equilibrium of organic molecules on the surface of Cu_2O–Cu. Hereafter, 0.03 ml of 30 wt% H_2O_2 was added into the solution. Then the photocatalytic reactions were carried out at room temperature by using a 90 W tungsten lamp as visible-light source. During the photocatalytic reaction, the circulating cooling water is used to avoid temperature rise. The reduction of the optical absorption peak of MB was determined from the UV–vis spectrophotometer. At different time intervals, 3 ml of solution was sampled for analysis. After centrifugation, the absorbance of the solution was measured. The degradation rate of dyes was calculated using the following equation:

$$D = \frac{(C_0 - C)}{C_0} \times 100\% = \frac{(A_0 - A)}{A_0} \times 100\%, \quad (1)$$

where *A* is the absorbency of the MB solution at 664 nm with different intervals and *C* is the concentration of dye solutions at different intervals.

An electrochemical analyzer (PAR Versastat 4-200) in a standard three-electrode system was used to perform the photoelectrochemical (PEC) measurements. The photocatalyst sample was coated onto the indium tin oxide (ITO) glass electrode. Then the ITO was sintered at 400 °C in vacuum for 1 h. The Cu_2O–Cu coated ITO, Pt and Ag/AgCl were used as the working electrode, counter electrode, and reference electrode in the electrochemical analyzer system, respectively. Na_2SO_4 aqueous solution (1 M) was used as the electrolyte in this system. The PEC responses were measured using a Xe lamp (300 W) with a light intensity of 100 mW/cm^2.

2.5. Radical quenching experiments

The method of the radical quenching experiments is the same as the photocatalytic activity tests. During the test, NBT with the concentration of 2.5×10^{-2} mM was added into the solution to quench the $\bullet O_2^-$ radicals. IPA with the volume percentage of 0.5% was added into the solution to quench the •OH radicals.

3. Results and discussion

3.1. Basic properties of the Cu_2O–Cu composites

3.1.1. Structure and morphology

The XRD patterns of Cu_2O–Cu composites with different reaction time are shown in Fig. 1. The diffraction peaks of S10 sample (curve a) can be indexed to a pure Cu_2O (space group *Pn*3*m*; JCPDS 05-0667). From curve b to curve f, the peaks corresponding to polycrystalline Cu (space group *Fm*3*m*; JCPDS 04-0836) emerges, indicating that the samples consist of Cu_2O and Cu phases. The relative intensity of the Cu peaks increases with the reaction time, showing an increase of Cu mass fraction. As the reaction time reaches 150 min (curve g), the Cu_2O diffraction peaks disappear, indicating that Cu_2O have been reduced to Cu completely. The XRD results reveal a conversion from Cu_2O to Cu with prolonged reaction time. In addition, the Cu_2O diffraction peaks of all samples have no observable shift, implying that no interstitial Cu atom distorts the Cu_2O lattice [40].

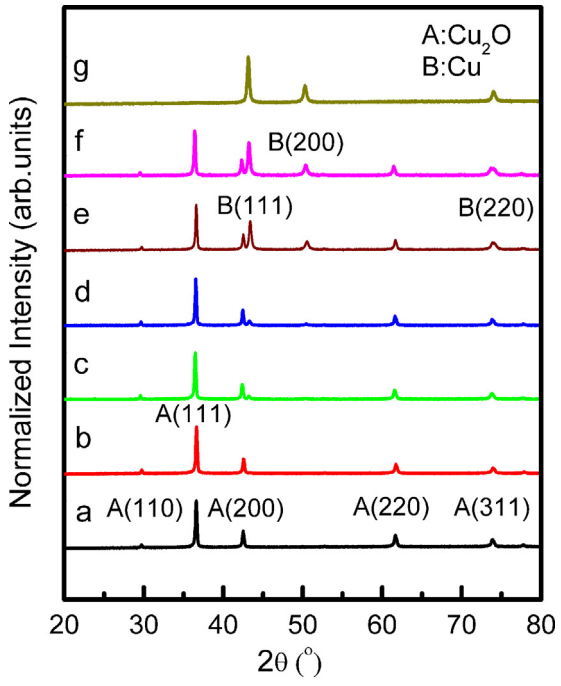

Fig. 1. The XRD patterns of Cu_2O–Cu composites. Curves a to g present the samples of S10, S20, S30, S40, S50, S60, and S150, respectively.

The morphologies of Cu_2O–Cu composites are characterized by SEM and shown in Fig. 2. It can be seen that the micron-sized Cu_2O are covered by Cu NPs with different coverage. Both the Cu_2O and Cu_2O–Cu have good monodispersity with uniform size and shape. In Fig. 2a, the S10 sample consists of aggregated Cu_2O microspheres with a diameter of ~1 μm. The surfaces of the microspheres are smooth without any small particles. At the reaction time of 20 min, some small Cu NPs appear on the Cu_2O surface as shown in Fig. 2b. The amount of the Cu NPs increases as accumulating the reaction time (from Fig. 2b–f). Besides, the size of Cu_2O microspheres reduces while that of the Cu NPs increases over the reaction time. On the other hand, the evolution of the Cu coverage density is noteworthy. For the S20, only a few particles exist on the Cu_2O surface. From 20 min to 50 min, the particles coverage area increases monotonically as shown in Fig. 2b–e. Especially for the S50 in Fig. 2e, the Cu_2O particles are completely enclosed by Cu NPs. However, as the reaction time extends to 60 min (S60), the Cu NPs fall off the Cu_2O surface as shown in Fig. 2f, inducing the Cu coverage density decreased significantly.

Fig. 3 displays the TEM bright field images of a typical sample (S40) measured at different magnifications. The low resolution images consist with the SEM images. The high resolution TEM (HRTEM) images show that the Cu_2O-microsphere surface is covered by lots of small NPs. The inset of Fig. 3d displays the fast Fourier transform (FFT) pattern of the selected areas in HRTEM images. The obtained FFT pattern indicates a regular spot pattern, presenting a single-crystalline nature of the particle. The set of diffraction spots can be indexed to the [1 0 1] zone axis of Cu, demonstrating the existence of the Cu on the Cu_2O surface.

3.1.2. Tuning optical properties by adjusting the coverage of Cu NPs

Optical properties were investigated by the UV–vis absorption spectra. As shown in Fig. 4, the S10 sample has a broadening absorption with the characteristic peak of Cu_2O at 490 nm [20,40] and the free exciton peak at 421 nm [41]. As the content of Cu NPs increases, the absorbance at ~490 nm increases first in the reaction time region of 10 to 40 min, and then decreases gradually in the region of 50 to 150 min. Specifically, for the S150, the absorbance at ~490 nm disappears completely, indicating that the Cu_2O have been completely reduced to Cu.

Beyond the absorption peak at ~490 nm, the S20 to S150 samples exhibit a broad absorbance centered at the wavelength of ~565 nm which becomes more pronounced with increasing Cu content. The ~565 nm absorbance of the pristine Cu (S150) is the most evident one in all samples. The analogous absorbance at around 565 nm has also been observed in other metallic Cu systems as a signature of the SPR [42–44]. It should be noticed that the Cu absorption spectra has a sloping background caused by the interband transitions [42,44]. Moreover, Fig. 4 indicates that the center of the SPR peak moves to the higher wavelength as the reaction time increases, exhibiting a red-shift. It has been demonstrated that the SPR peak position and the plasmon field intensity depend on the shape and size of the nanoparticles as well as the dielectric of the surrounding medium [45]. According to the SEM images in Fig. 2, the Cu particle grows up with increasing the reaction time. Therefore, the red-shift of the SPR peak over the reaction time may be attributed to the increase of the size of the Cu NPs [46].

Now we return to discuss the evolution of the ~490 nm absorbance. First, the absorbance gets stronger from S10 to S40. This may be caused by the enhancement of Cu SPR, which is added

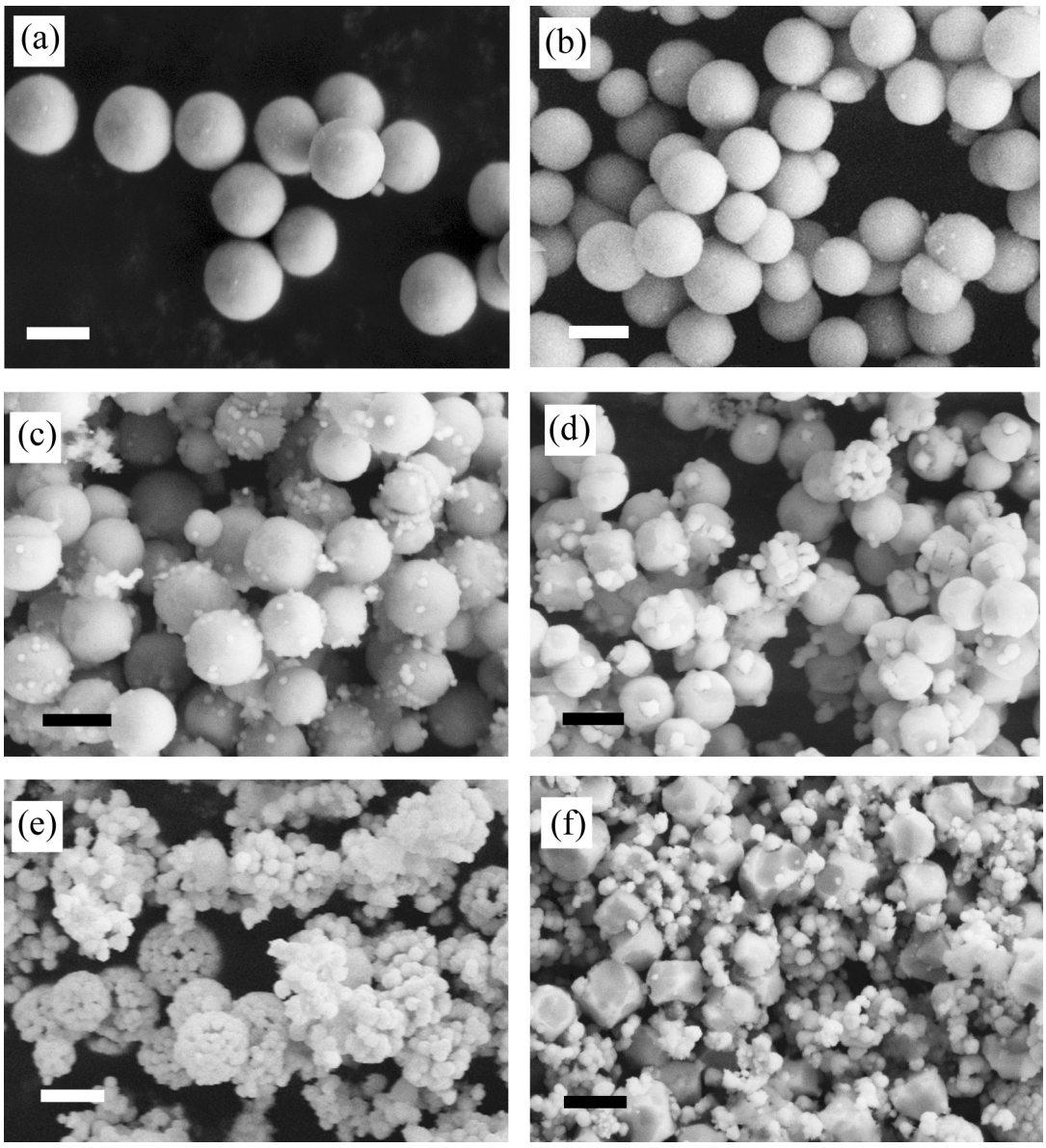

Fig. 2. The SEM images of the Cu_2O–Cu samples of (a) S10, (b) S20, (c) S30, (d) S40, (e) S50, and (f) S60. Scalebar: 1 μm.

to the Cu_2O peak at ~490 nm. Moreover, Cu NPs on the Cu_2O surface will increase the reflection of the transmission light to improve its re-absorbance. Second, from S40 to S150, the absorption intensity gradually declines to zero. As exhibited in Fig. 2d–f, the Cu coverage density increases with the reaction time, and the Cu_2O particles are covered by Cu NPs completely for S50. Consequently, the number of the photon arriving at the Cu_2O surface is reduced and the light absorption intensity of Cu_2O is decreased accordingly. As the reaction time is longer than 60 min, the Cu NPs start to fall off the Cu_2O surface. However, since the reaction time is rather long, most of Cu_2O have been reduced to Cu. As a result, the absorption of Cu_2O gets weaker obviously. For the sample of S150, the Cu_2O have been reduced completely, thus, the absorption peaks of Cu_2O disappeared.

3.2. Degradation of MB

3.2.1. Effects of the Cu NPs on MB degradation

In order to study the photocatalytic activity of the Cu_2O–Cu composites, the degradation of MB in aqueous solution under the visible-light was performed. During the test, the degradation rate of MB was monitored by the UV–vis absorption spectrum. First, the concentration evaluation of the pure MB solution was measured under the photo irradiation. As shown in Fig. 5, the concentration of the MB solution is almost unchanged after irradiated for 60 min. Besides the pure MB degradation, all other experiments were carried out in the presence of H_2O_2. The commercial TiO_2 (P25) and the H_2O_2 were used as the references. The inset of Fig. 5a shows absorption spectrum of MB at various visible-light irradiation times in the presence of S40. It can be seen that the MB has a sharp absorption peak around 664 nm whose intensity reduces over the irradiation time. After irradiating for 60 min, the peak almost vanishes suggesting that the MB is degraded.

Fig. 5a presents the concentration ratio C/C_0 of MB solution (the ratio of the MB concentration C to the original MB concentration C_0) as a function of irradiation time. The curve S10 shows the degradation of MB by Cu_2O, which leads to 52% degradation rate of MB after irradiating for 60 min. However, the degradation rate is only 30% and 28% for P25 and H_2O_2, respectively. After introducing Cu NPs to the Cu_2O surface, the activity of photodegrading MB

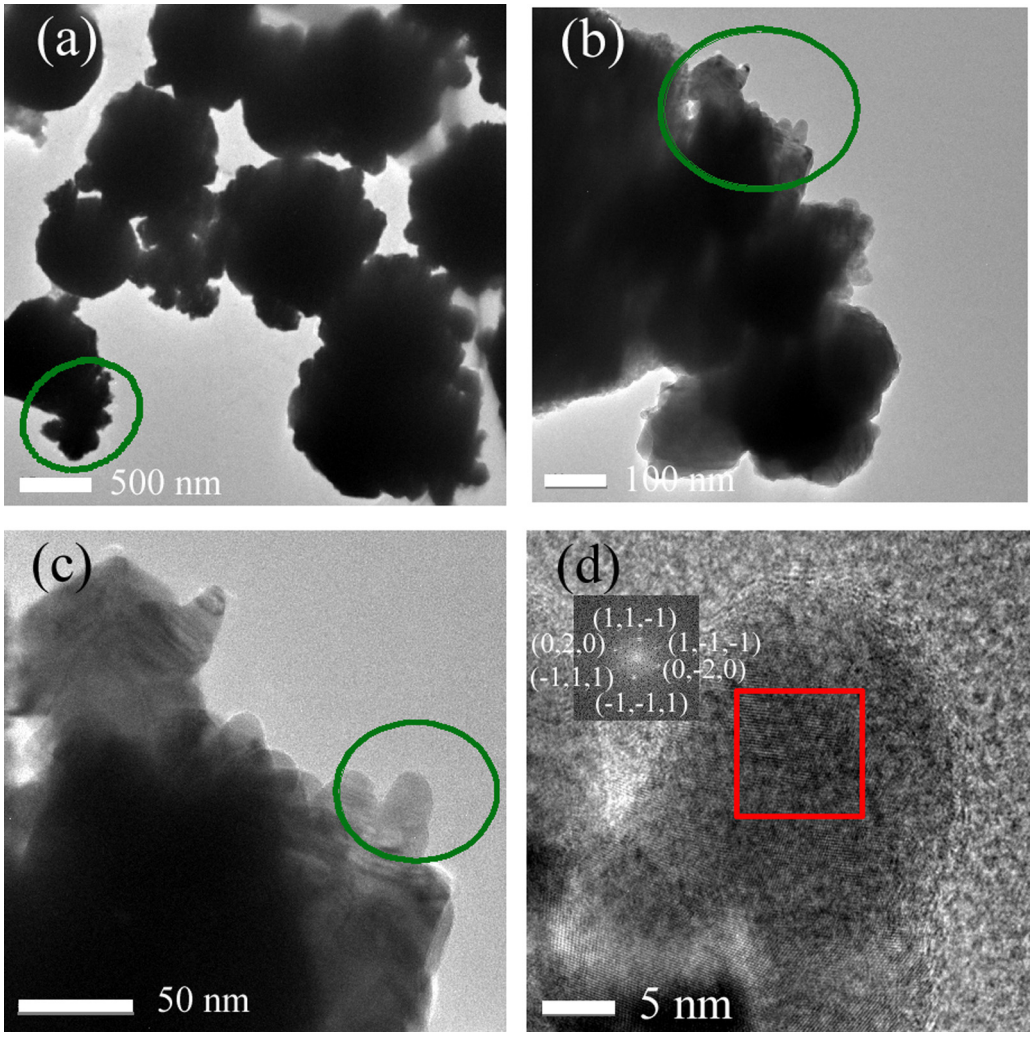

Fig. 3. TEM bright field images of S40 sample. (a)–(d) With different magnifications. The circles indicate the measurement areas. The inset of (d) is the fast FFT images of the selected areas.

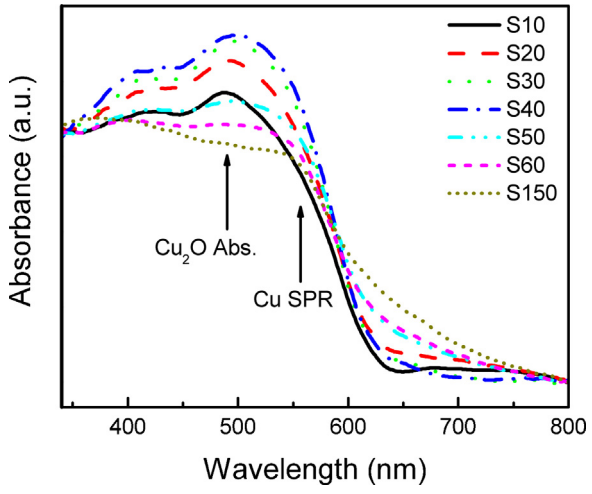

Fig. 4. The UV–vis absorption spectra of Cu_2O–Cu composites.

is further improved. With increasing Cu NPs content, the degradation rate increases and reaches the maximum of 88% for S40 after irradiating for 60 min, and then decreases gradually with further increasing Cu NPs content. The trend is illustrated in Fig. 5b through the histogram. Interestingly, the maximum degradation rate is well consistent with the absorption spectrum in Fig. 4, in which the S40 has the strongest absorption at the visible-light range due to the SPR. The result indicates that the SPR contributes a crucial effort to improve the photocatalytic activity. Besides, it should be mentioned that the photosensitization role of dyes can be ruled out since the degradation rate for both S10 and P25 are low and these photosensitization role should be constant for all samples.

It has been reported that the photoexcited plasmonic energy can be transferred from the SPR metal to the interfaced Cu_2O in three ways, i.e., the local electromagnetic field enhancement (LEMF) for the charge separation, the plasmon-induced resonant energy transfer (PIRET) [39], and the direct electron transfer (DET) of the hot electrons [47]. Through these ways, the generation of the electron–hole pairs will be improved greatly. With further increasing the reaction time, the Cu NPs break away from Cu_2O, resulting in a reduction of the SPR contribution. Besides, since the content of Cu_2O decreases remarkably, the degradation rate of MB is decreased from S40 to S60. The overall trend demonstrates an enhanced photocatalytic activity stemming from the presence of Cu NPs, and the S40 sample displays the highest photocatalytic performance.

The role of Cu NPs on the photocatalysis can further be understood by studying the response of the photodegradation efficiency on the special wavelength of the incident light. The narrow

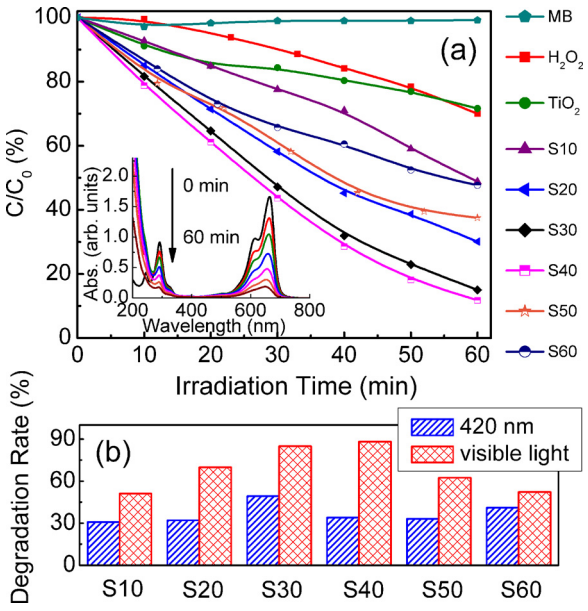

Fig. 5. (a) Photodegradation of MB vs. irradiation time for the Cu_2O–Cu composites, TiO_2 and H_2O_2. The inset of (a) is the absorption spectrum of MB solution at different irradiation time in the presence of S40. (b) The MB degradation rate over the Cu_2O–Cu specimens irradiated by 420 nm and visible light for 60 min, respectively.

band-pass optical filters were used to control the wavelength of the light. Since the SPR only appeared at around 565 nm, if the sample is irradiated by the light with lower wavelength than 565 nm, the effect of the SPR can be excluded. The 420 nm filter is selected in the measurement. Besides, in order to provide sufficient light intensity, the 300 W xenon lamp was used as the light source. Fig. 5b demonstrates the degradation rate of MB for different samples irradiated by the 420 nm light. It shows that when the SPR effect is excluded by the 420 nm light, the photocatalytic activity exhibits no significant Cu content dependency, indicating that the SPR effect plays a key role in MB degradation under the visible-light.

The role of Cu NPs on the separation of the photogenerated carrier during the photocatalysis was investigated by the electrochemical impedance spectroscopy (EIS) measurements. The typical Nyquist plots of the EIS are shown in Fig. S1 in the Supplementary data. In the EIS plots, only one semicircle was observed for each sample, which is associated with the charge transfer process [48]. It is known that the arcs in the Nyquist plot reflect charge-transfer resistance at the surface of the electrode. Obviously, with increasing the Cu content, the arc radius of the EIS spectra decreases, indicating that a fast interfacial charge transfer and an effective separation of the photogenerated electron–hole pairs have occurred with the aid of Cu NPs [49–53].

3.2.2. *Effects of the H_2O_2 and dark catalytic reaction*

It is worth noting that all the photodegradation experiments above were performed in the presence of the H_2O_2 which is crucial in the high efficiency photocatalysis. The role of H_2O_2 is studied through series of comparative experiments as listed in Table 1 (from 1# to 6# specimen). The photographs of the obtained MB solutions under different experimental conditions are demonstrated in Fig. 6.

Fig. 6a–d show the results under the visible-light. It can be seen that the MB solutions containing only Cu_2O–Cu (2#) or only H_2O_2 (3#) still keep in blue after irradiated by visible-light for 60 min, exhibiting faint fading comparing with the original MB solution (1#). While, the solution containing both Cu_2O–Cu and H_2O_2 (4#) becomes almost colorless after irradiating, consisting with the UV–vis absorption spectrum results in Section 3.2.1. Therefore, it can be inferred that both Cu_2O–Cu and H_2O_2 are necessary for the

Table 1
List of the catalytic conditions for different specimens.

Sample	Visible-light	Cu_2O–Cu (S40)	H_2O_2	Period	NBT	IPA
1#	N	N	N	–	N	N
2#	Y	Y	N	60 min	N	N
3#	Y	N	Y	60 min	N	N
4#	Y	Y	Y	60 min	N	N
5#	N	Y	Y	Over night	N	N
6#	N	N	Y	Over night	N	N
7#	Y	Y	Y	60 min	Y	N
8#	N	Y	Y	Over night	Y	N
9#	Y	Y	Y	60 min	N	Y
10#	N	Y	Y	Over night	N	Y

high efficiency photodegradation. It has been known that if the Cu_2O is irradiated by the visible-light, it will be excited to generate the electron–hole (e^-–h^+) pairs. The photogenerated e^- and h^+ can react with the oxidants and reducers separately to produce active oxidative radicals such as superoxide radical ($\bullet O_2^-$) and hydroxyl radical ($\bullet$OH) to degrade the organic pollutant. However, the top of the Cu_2O valance band is higher than the oxidation potential of H_2O so that the h^+ can't react with OH^- to form $\bullet$OH. The introduction of Cu will further raise the valance band of Cu_2O because the work function of Cu is smaller than that of the Cu_2O. So the Cu_2O–Cu composite can't generate $\bullet$OH effectively through the photogenerated holes. In addition, the dissolved oxygen in the water is too trace to effectively produce $\bullet O_2^-$. Therefore, the Cu_2O–Cu photocatalyst without H_2O_2 has poor activity. The introduction of H_2O_2 provides a large amount of O_2 involving the reaction of producing oxidative $\bullet O_2^-$. The $\bullet O_2^-$ radicals further react with H_2O_2 to form $\bullet$OH, which has strong oxidative capacity. Besides, the H_2O_2 can also react with photogenerated electrons directly to produce $\bullet$OH [54].

To gain further insights into the role of H_2O_2, the comparative experiments were carried out in dark and shown in Fig. 6e and f. In the presents of both Cu_2O–Cu and H_2O_2, the MB solution fades significantly and produces numerous of bubbles in dark (5#), indicating that the Cu_2O–Cu–H_2O_2 system enables MB degradation in dark. However, the degradation efficiency of MB in dark (5#) is lower than that in the visible-light (4#). On the other hand, the H_2O_2 alone (6#) doesn't degrade the MB in dark, implying a

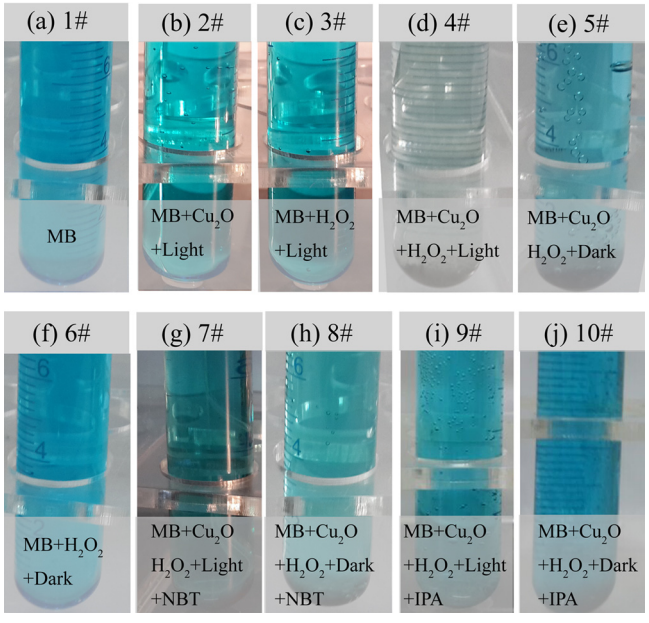

Fig. 6. Photographs of MB solutions under different catalytic conditions.

synergistic effect of Cu_2O–Cu and H_2O_2 for degrading MB in dark. The phenomenon of degrading MB in dark is interesting since there are no photogenerated electron and hole to generate the oxidative radicals. Recently, the similar dark catalysis phenomena have also been observed in the TiO_2–H_2O_2 [55] and BiOBr–H_2O_2 [54] system, which were attributed to the Fenton-like behaviors. It is known that the Fenton reaction, which is one of the most widely applied advanced catalytic method for degrading the organic pollutants by generating the •OH radicals [56], takes place in the system containing both ferrous and H_2O_2. The mechanism of the Fenton-like reaction in the Cu_2O–Cu–H_2O_2 system may be similar with the Fe^{2+} system following the equations [57,58]:

$$Cu^{+} + H_2O_2 \rightarrow Cu^{2+} + \bullet OH + OH^{-} \quad (2)$$

$$Cu^{2+} + H_2O_2 \rightarrow Cu^{+} + \bullet O_2H + H^{+} \quad (3)$$

The Cu^+ ions react with H_2O_2 to generate •OH radicals, meanwhile the Cu^{2+} ions prefer to produce Cu^+. As a result, Cu^+ amount is maintained and only H_2O_2 is consumed during the whole reaction. Actually, the existence of the Cu^+ ions and Cu^{2+} ions can be proved by the XPS measurements. In Fig. S2 in the Supplementary data, it shows the Cu 2p XPS spectrum for the samples of S10, S40, S60 and S150. Both the Cu $2p_{1/2}$ and Cu $2p_{3/2}$ peaks include the chemical states of Cu^{2+} and Cu^{1+} (Cu^0). The peaks located at the binding energy of ~932.6 eV and 952.2 eV are characteristics of Cu^{1+}. The broadening parts of both two peaks at the binding energy of ~932.2 eV and 953.8 eV are related to the Cu^{2+} on the sample surface. In the next part, the radical quenching experiments will prove the generation of the •OH radicals in the solution, which will be the evidence for the Fenton-like reaction.

3.2.3. Radical quenching experiments

To address the mechanism of the high photocatalytic activity, the quenching experiments for the oxidative radicals in the catalytic process were carried out as listed in Table 1 (7#–10# specimen). First, NBT is used to quench the $\bullet O_2^-$ radicals (7# and 8# in Table 1). Under the visible-light in Fig. 6g, comparing with the solution without the quenching agent (4#), the addition of the $\bullet O_2^-$ quenching agent (7#) makes the photocatalyst deactivated evidently, indicating that the $\bullet O_2^-$ radicals play a crucial role for MB photodegradation. On the other hand, in darkness as shown in Fig. 6h, the solution added NBT (8#) has no evident color difference compared with the solution without NBT (5#), revealing that the quenching of $\bullet O_2^-$ radicals has no remarkable effect on the dark catalysis. Therefore, the dark catalysis is not dominated by the $\bullet O_2^-$ radicals.

Second, the effects of the •OH radicals on degrading MB are detected using IPA as a quenching agent of •OH radicals in presence and absence of visible-light (9# and 10# in Table 1), respectively. As shown in Fig. 6i, after quenching •OH radicals under the visible-light (9#), the degrading speed decreases greatly compared with the solution without quenching agent (4#). It means that the •OH radicals also contribute to the MB photodegradation. While for the dark catalytic reaction with the IPA in Fig. 6j, the solution (10#) keeps in blue and shows no fade overnight, indicating that when •OH radicals are quenched, the dark catalytic ability of the Cu_2O–Cu–H_2O_2 is lost. So it can be deduced that the dark catalytic reaction is dominated by •OH radicals, which is in accordance with Eq. (2) in Section 3.2.2 for the Fenton-like reactions.

3.2.4. The repeated experiment

The repeated experiment of the sample is conducted through the degradation of MB under the visible-light using S40. Every measurement cycle was for 60 min with new prepared MB solution for each cycle. The results are shown in Fig. S3 in the Supplementary data. It shows that the degradation efficiency decreases with increase the cycling time from 1 to 3 cycles. While after 3 cycles, the degradation efficiency becomes stable with the cycling time. The stability of these Cu_2O–Cu photocatalysts needs to be further improved in the future.

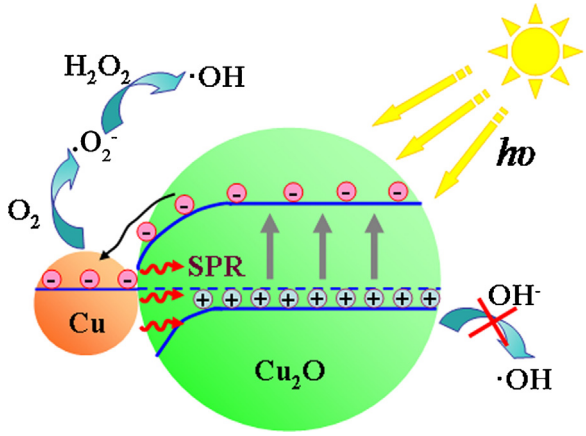

Fig. 7. Scheme diagram of the proposed •OH radical generation process in the Cu_2O–Cu–H_2O_2 system and the energy band alignment.

3.2.5. Mechanism of the degradation

According to the results above, the mechanism of degradation of MB in the Cu_2O–Cu–H_2O_2 systems can be illustrated by Fig. 7.

Cu_2O is a semiconductor with the bandgap of 2.17 eV, absorbing the visible-light to generate electron–hole pairs. The photogenerated electron–hole pairs have high activity, which may react with O_2, H_2O_2, OH^-, and etc. to form the oxidative radicals such as $\bullet O_2^-$ and •OH, governing the photocatalytic procedure.

The presence of Cu NPs promotes the photocatalysis. The UV–vis absorption spectrum shows that the Cu NPs exhibit the SPR effect, which increases the visible-light absorbance to improve the utilizing efficiency of the visible-light. Besides, the energy can be transferred to semiconductor Cu_2O to further improve the generation of the electron and hole. Moreover, because of the low work function and good conductive ability for Cu, the photogenerated electrons can easily transfer to the Cu NPs to decrease the recombination of the photogenerated electrons and holes [59], which have been proved by the EIS measurements. Besides, the Cu NPs present at the surface of Cu_2O, ensuring that both photogenerated electrons and holes are on the surface to improve the photocatalytic efficiency.

The role of H_2O_2 can be discussed on two hands. During the photocatalysis, since the top of the valance band is higher than the oxidation potential of the H_2O, the forming of the •OH through H_2O directly is forbidden. Therefore, the adding of H_2O_2 is necessary because it provides O_2 to produce the $\bullet O_2^-$ and further transfers into •OH, or reacts with photogenerated electrons directly to form •OH. During the dark catalysis, H_2O_2 provides an environment for the Fenton-like reaction in the presence of the multiple valences of Cu. So the system can degrade the MB in the darkness. It should be mentioned that according to the radical quenching experiments, both the $\bullet O_2^-$ and the •OH radicals contribute to the MB photodegradations. During the dark catalysis, only the •OH radicals dominate the reaction.

4. Conclusion

In this research, nano-Cu-covered Cu_2O microspheres have been synthesized and utilized in the organic pollutant degradation. The optical results reveal that the Cu NPs introduce the SPR effect into the catalyst. The degrading experiments display that with the existence of Cu NPs, the photodegradation rate improves

from 52% for S10 sample to the maximum of 88% for S40 sample under the visible-light irradiation. Furthermore, by studying the photocatalytic efficiency under the special wavelength (420 nm) of the incident light, it is confirmed that the SPR plays a crucial role on the improvement of the photocatalytic activity. Besides, in the presence of H_2O_2, a dark catalytic activity is observed due to the Fenton-like reaction. The mechanisms of both photocatalysis and dark catalysis were discussed through the comparative experiments. It proves that both $\bullet O_2^-$ and •OH radicals contribute to the degradation during the photocatalytic process, while the dark catalytic performance is only governed by the •OH radicals. In conclusion, with the aid of SPR and dark catalysis, the Cu_2O based photocatalytic behaviors are significantly improved.

Acknowledgements

This work was supported by the following grants: National Basic Research Program of China (973 Program with no. 2014CB931703), National Natural Science Foundation of China (nos. 51101088, 51171082, 11304161), Tianjin Natural Science Foundation (nos. 13JCQNJC02800, 13JCYBJC41100, 14JCZDJC37700), and Specialized Research Fund for the Doctoral Program of Higher Education (no. 20110031110034).

Appendix A. Supplementary data

Supplementary data associated with this article can be found, in the online version, at http://dx.doi.org/10.1016/j.apsusc.2015.12.238.

References

[1] A. Fujishima, K. Honda, Electrochemical photolysis of water at a semiconductor electrode, Nature 238 (1972) 37–38.
[2] X. Chen, S. Shen, L. Guo, S. Mao, Semiconductor-based photocatalytic hydrogen generation, Chem. Rev. 110 (2010) 6503–6570.
[3] R. Asahi, T. Morikawa, T. Ohwaki, K. Aoki, Y. Taga, Visible-light photocatalysis in nitrogen-doped titanium oxides, Science 293 (2001) 269–271.
[4] T.P. Yoon, M.A. Ischay, J. Du, Visible light photocatalysis as a greener approach to photochemical synthesis, Nat. Chem. 2 (2010) 527–532.
[5] J. Tang, Z. Zou, J. Ye, Efficient photocatalysis decomposition of organic contaminants over $CaBi_2O_4$ under visible-light irradiation, Angew. Chem. Int. Ed. 43 (2004) 4463–4466.
[6] X. Chen, S.S. Mao, Titanium dioxide nanomaterials: synthesis, properties, modifications, and applications, Chem. Rev. 107 (2007) 2891–2959.
[7] X. Li, P. Liu, Y. Mao, M. Xing, J. Zhang, Preparation of homogeneous nitrogen-doped mesoporous TiO_2 spheres with enhanced visible-light photocatalysis, Appl. Catal., B: Environ. 164 (2015) 329–359.
[8] Z. Zhao, H. Tan, H. Zhao, Y. Lv, L.-J. Zhou, Y. Song, Z. Sun, Reduced TiO_2 rutile nanorods with well-defined facets and their visible-light photocatalytic activity, Chem. Commun. 50 (2014) 2755–2757.
[9] L. Vayssieres, C. Sathe, S.M. Butorin, D.K. Shuh, J. Nordgren, J. Guo, One-dimensional quantum-confinement effect in α-Fe_2O_3 ultrafine nanorod arrays, Adv. Mater. 17 (2005) 2320–2323.
[10] P. de Mayo, K. Muthuramu, W.K. Wong, Surface photochemistry: efficient photocatalysis by CdS supported on a solid surface, Catal. Lett. 10 (1991) 71–82.
[11] Y. Park, K.J. McDonald, K.S. Choi, Progress in bismuth vanadate photoanodes for use in solar water oxidation, Chem. Soc. Rev. 42 (2013) 2321–2337.
[12] D. Chen, J. Ye, Hierarchical WO_3 hollow shells: dendrite, sphere, dumbbell, and their photocatalytic properties, Adv. Funct. Mater. 18 (2008) 1922–1928.
[13] J.Y. Ho, M.H. Huang, Synthesis of submicrometer-sized Cu_2O crystals with morphological evolution from cubic to hexapod structures and their comparative photocatalytic activity, J. Phys. Chem., C 113 (2009) 14159–14164.
[14] L. Xiong, T.W. Ng, Y. Yu, D. Xia, H.Y. Yip, G. Li, T. An, H. Zhao, P.K. Wong, N-tpye Cu_2O film for photocatalytic and photoelectrocatalytic process: its stability and inactivation of *E. coli*, Electrochim. Acta 153 (2015) 583–593.
[15] Y. Zhang, B. Deng, T. Zhang, D. Gao, A.-W. Xu, Shape effects of Cu_2O nanocrystals and their properties, J. Phys. Chem., C 114 (2010) 5073–5079.
[16] C.-H. Kuo, C.-H. Chen, M.H. Huang, Seed-mediated synthesis of monodispersed Cu_2O nanocubes with five different size ranges from 40 to 420 nm, Adv. Funct. Mater. 17 (2007) 3773–3780.
[17] Y.-G. Zhang, L.-L. Ma, J.-L. Li, Y. Yu, In situ Fenton reagent generated from TiO_2/Cu_2O composite film: a new way to utilize TiO_2 under visible light irradiation, Environ. Sci. Technol. 41 (2007) 6264–6269.
[18] C. Xu, L. Cao, G. Su, W. Liu, H. Liu, Y. Yu, X. Qu, Preparation of ZnO/Cu_2O compound photocatalyst and application in treating organic dyes, J. Hazard. Mater. 176 (2010) 807–813.
[19] J.G. Hou, C. Yang, H.J. Cheng, S.Q. Jiao, O. Takeda, H.M. Zhu, High-performance p-Cu_2O/n-TaON heterojunction nanorod photoanodes passivated with an ultrathin carbon sheath for photoelectrochemical water splitting, Energy Environ. Sci. 7 (2014) 3758–3768.
[20] Y. Pan, S. Deng, L. Polavarapu, N. Gao, P. Yuan, C.H. Sow, Q. Xu, Plasmon-enhanced photocatalytic properties of Cu_2O nanowire-Au nanoparticle assemblies, Langmuir 28 (2012) 12304–12310.
[21] J. Li, S.K. Cushing, J. Bright, F. Meng, T.R. Senty, P. Zheng, A.D. Bristow, N. Wu, Ag@Cu_2O core–shell nanoparticles as visible-light plasmonic photocatalysis, ACS Catal. 3 (2013) 47–51.
[22] M.A. Mahmoud, W. Qian, M.A. El-Sayed, Following charge separation on the nanoscale in Cu_2O–Au nanoframe hollow nanoparticles, Nano Lett. 11 (2011) 3285–3289.
[23] F. Shao, J. Sun, L. Gao, J. Luo, Y. Liu, S. Yang, High efficiency semiconductor–liquid junction solar cells based on Cu/Cu_2O, Adv. Funct. Mater. 22 (2012) 3907–3913.
[24] S. Xu, S. Sun, G. Chen, X. Song, Rapid room-temperature fabrication of Cu_2O–Au core–shell nanospheres, J. Cryst. Growth 311 (2009) 2742–2745.
[25] Y. Zheng, C. Chen, Y. Zhan, X. Lin, Q. Zheng, K. Wei, J. Zhu, Photocatalytic activity of Ag/ZnO heterostructure nanocatalyst: correlation between structure and property, J. Phys. Chem., C 112 (2008) 10773–10777.
[26] H. Zhu, X. Ke, X. Yang, S. Sarina, H. Liu, Reduction of nitroaromatic compounds on supported gold nanoparticles by visible and ultraviolet light, Angew. Chem. Int. Ed. 49 (2010) 9657–9661.
[27] S. Navalon, M. de Miguel, R. Martin, M. Alvaro, H. Garcia, Enhancement of the catalytic activity of supported gold nanoparticles for the Fenton reaction by light, J. Am. Chem. Soc. 133 (2011) 2218–2226.
[28] P. Christopher, H. Xin, S. Linic, Visible-light-enhanced catalytic oxidation reactions on plasmonic silver nanostructures, Nat. Chem. 3 (2011) 467–472.
[29] X. Chen, H.-Y. Zhu, J.-C. Zhao, Z.-F. Zheng, X.-P. Gao, Visible-light-driven oxidation of organic contaminants in air with gold nanoparticle catalysts on oxide supports, Angew. Chem. Int. Ed. 47 (2008) 5353–5356.
[30] S. Linic, P. Christopher, D.B. Ingram, Plasmonic-metal nanostructures for efficient conversion of solar to chemical energy, Nat. Mater. 10 (2011) 911–921.
[31] C. Clavero, Plasmon-induced hot-electron generation at nanoparticle/metal–oxide interfaces for photovoltaic and photocatalytic devices, Nat. Photonics 8 (2014) 95–103.
[32] R. Jia, G. Lin, D. Zhao, Q. Zhang, X. Lin, N. Gao, D. Liu, Sandwich-structured Cu_2O photodetectors enhanced by localized surface plasmon resonances, Appl. Surf. Sci. 332 (2015) 340–345.
[33] M. Mahanti, D. Basak, Cu/ZnO nanorods' hybrid showing enhanced photoluminescence properties due to surface plasmon resonance, J. Lumin. 145 (2014) 19–24.
[34] K.-Y. Pan, Y.-F. Liang, Y.-C. Pu, Y.-J. Hsu, J.-W. Yeh, H.C. Shih, Studies on the photocatalysis of core–shelled SiO_2–Ag nanospheres by controlled surface plasmon resonance under visible light, Appl. Phys. Lett. 311 (2014) 399–404.
[35] K.H. Leong, B.L. Gan, S. Ibrahim, P. Saravanan, Synthesis of surface plasmon resonance (SPR) triggered Ag/TiO_2 photocatalyst for degradation of endocrine disturbing compounds, Appl. Surf. Sci. 319 (2014) 128–135.
[36] Y. Wang, J. Yu, W. Xiao, Q. Li, Microwave-assisted hydrothermal synthesis of graphene based Au–TiO_2 photocatalysts for efficient visible-light hydrogen production, J. Mater. Chem., A 2 (2014) 3847–3855.
[37] M. Tahir, B. Tahir, N.A.S. Amin, Gold-nanoparticle-modified TiO_2 nanowires for plasmon-enhanced photocatalytic CO_2 reduction with H_2 under visible light irradiation, Appl. Surf. Sci. 356 (2015) 1289–1299.
[38] M. Murdoch, G.I.N. Waterhouse, M.A. Nadeem, J.B. Metson, M.A. Keane, R.F. Howe, J. Llorca, H. Idriss, The effect of gold loading and particle size on photocatalytic hydrogen production from ethanol over Au/TiO_2 nanoparticles, Nat. Chem. 3 (2011) 489–492.
[39] S.K. Cushing, J. Li, F. Meng, T.R. Senty, S. Suri, M. Zhi, M. Li, A.D. Bristow, N. Wu, Photocatalytic activity enhanced by plasmonic resonant energy transfer from metal to semiconductor, J. Am. Chem. Soc. 134 (2012) 15033–15041.
[40] J. Kou, A. Saha, C.B. Stamper, R.S. Varma, Inside-out core–shell architecture: controllable fabrication of Cu_2O@Cu with high activity for the Sonogashira coupling reaction, Chem. Commun. 48 (2012) 5862–5864.
[41] L. Liu, S. Lin, J. Hu, Y. Liang, W. Cui, Plasmon-enhanced photocatalytic properties of nano Ag@AgBr on single-crystalline octahedral Cu_2O (1 1 1) microcrystals composite photocatalyst, Appl. Surf. Sci. 330 (2015) 94–103.
[42] A. Marimuthu, J. Zhang, S. Linic, Tuning selectivity in propylene epoxidation by plasmon mediated photo-switching of Cu oxidation state, Science 339 (2013) 1590–1593.
[43] K.P. Rice, E.J. Walker, M.P. Stoykovich, A.E. Saunders, Solvent-dependent surface plasmon response and oxidation of copper nanocrystals, J. Phys. Chem., C 115 (2011) 1793–1799.
[44] H. Wang, F. Tam, N.K. Grady, N.J. Halas, Cu nanoshells: effects of interband transitions on the nanoparticle plasmon resonance, J. Phys. Chem., B 109 (2005) 18218–18222.
[45] M.A. Mahmoud, M.A. El-Sayed, Gold nanoframes: very high surface plasmon fields and excellent near-infrared sensors, J. Am. Chem. Soc. 132 (2010) 12704–12710.

[46] D.Y. Liu, S.Y. Ding, H.X. Lin, B.J. Liu, Z.Z. Ye, F.R. Fan, B. Ren, Z.Q. Tian, Distinctive enhanced and tunable plasmon resonant absorption from controllable Au@Cu_2O nanoparticles: experimental and theoretical modeling, J. Phys. Chem., C 116 (2012) 4477–4483.
[47] Y. Tian, T. Tatsuma, Mechanisms and applications of plasmon-induced charge separation at TiO_2 films loaded with gold nanoparticles, J. Am. Chem. Soc. 127 (2005) 7632–7637.
[48] G. Wang, S. Chen, H. Yu, X. Quan, Integration of membrane filtration and photoelectrocatalysis using a TiO_2/carbon/Al_2O_3 membrane for enhanced water treatment, J. Hazard. Mater. 299 (2015) 27–34.
[49] J. Low, J. Yu, Q. Li, B. Cheng, Enhanced visible-light photocatalytic activity of plasmonic Ag and grapheme co-modified Bi_2WO_6 nanosheets, Phys. Chem. Chem. Phys. 16 (2014) 1111–1120.
[50] M. Li, W. Luo, D. Cao, X. Zhao, Z. Li, T. Yu, Z. Zou, A cocatalyst-loaded Ta_3N_5 photoanode with a high solar photocurrent for water splitting upon facile removal of the surface layer, Angew. Chem. Int. Ed. 52 (2013) 1–6.
[51] Y. Hou, F. Zuo, A.P. Dagg, J. Liu, P. Feng, Branched WO_3 nanosheet array with layered C_3N_4 heterojunctions and CoO_x nanoparticles as a flexible photoanode for efficient photoelectrochemical water oxidation, Adv. Mater. 26 (2014) 5043–5049.
[52] B. Klahr, S. Gimenez, F. Fabregat-Santiagl, T. Hamann, J. Bisquert, Water oxidation at hematite photoelectrodes: the role of surface states, J. Am. Chem. Soc. 134 (2012) 4294–4302.
[53] X. Chang, T. Wang, P. Zhang, J. Zhang, A. Li, J. Gong, Enhanced surface reaction kinetics and charge separation of p–n heterojunction Co_3O_4/$BiVO_4$ photoanodes, J. Am. Chem. Soc. 137 (2015) 8356–8359.
[54] L. Li, L. Ai, C. Zhang, J. Jiang, Hierarchical {0 0 1}-faceted BiOBr microspheres as a novel biomimetic catalyst: dark catalysis towards colorimetric biosensing and pollutant degradation, Nanoscale 6 (2014) 4627–4634.
[55] D.S. Luis, F.M.T.-L. Sébastien, O.H. Eli, K. André, S. Einar, J.H. Håvard, TiO_2 suspension exposed to H_2O_2 in ambient light or darkness: degradation of methylene blue and EPR evidence for radical oxygen species, Appl. Catal., B: Environ. 142–143 (2013) 662–667.
[56] M. Hartmann, S. Kullmann, H. Keller, Wastewater treatment with heterogeneous Feton-tpye catalysts based on porous materials, J. Mater. Chem. 20 (2010) 9002–9017.
[57] L.L. Zhang, Y.L. Nie, C. Hu, J.H. Qu, Enhanced Fenton degradation of Rhodamine B over nanoscaled Cu-doped $LaTiO_3$ perovskite, Appl. Catal., B: Environ. 125 (2012) 418–424.
[58] Y. Wang, H. Zhao, M. Li, J. Fan, G. Zhao, Magnetic ordered mesoporous copper ferrite as a heterogeneous Fenton catalyst for the degradation of imidacloprid, Appl. Catal., B: Environ. 147 (2014) 534–545.
[59] W.W. Lu, S.Y. Gao, J.J. Wang, One-pot synthesis of Ag/ZnO self-assembled 3D hollow microspheres with enhanced photocatalytic performance, J. Phys. Chem., C 112 (2008) 16792–16800.